Applied Catalysis B: Environmental 245 (2019) 623–634

Contents lists available at ScienceDirect

Applied Catalysis B: Environmental

journal homepage: www.elsevier.com/locate/apcatb

Ceria-based nanoflake arrays integrated on 3D cordierite honeycombs for efficient low-temperature diesel oxidation catalyst

Wenxiang Tang[a], Xingxu Lu[a], Fangyuan Liu[a], Shoucheng Du[a], Junfei Weng[a], Son Hoang[a], Sibo Wang[a], Chang-Yong Nam[b,*], Pu-Xian Gao[a,*]

[a] Department of Materials Science and Engineering & Institute of Materials Science, University of Connecticut, Storrs, CT 06269-3136, USA
[b] Center for Functional Nanomaterials, Brookhaven National Laboratory, Upton, NY 11973, USA

ARTICLE INFO

Keywords:
CeO_2
Nano-flake array
Monolithic catalyst
Pt nanoparticles
Low-Temperature diesel oxidation catalyst

ABSTRACT

A new, surfactant-free hydrothermal method has been developed for the growth of CeO_2-based nanoflake arrays onto three-dimensional-channeled cordierite honeycomb substrates. Herein, a leaching-crystallization mechanism was proposed where the hydrothermal reaction, only involving cerium nitrate and water, leached the cordierite surface slightly and induced the formation of CeO_2 nanoparticles subsequently. Further continued reaction reincorporated Al and Si atoms leached from cordierite into CeO_2, finally recrystallizing Ce-Al-Si composite nanoflake structures. By using atomic layer deposition process, well-dispersed, size-controlled Pt nanoparticles were uniformly decorated on the CeO_2-based nanoflakes to form the Pt/ CeO_2 nano-array-based monolithic catalyst. Despite 5-50 times reduction in the active material usage compared with the traditional wash-coated catalyst, the Pt/CeO_2 nano-array monolithic catalyst exhibited good catalytic oxidation activities over various individual gases, such as propylene, propane, CO, and NO oxidation, with 90% conversion efficiencies at temperatures below 200 °C. Under the simulated exhaust condition of low-temperature diesel combustion (LTC-D) developed by US DRIVE, the monolithic catalyst with low Pt loading (˜1 g/l) exhibits 90% conversion of catalytic oxidation over CO and hydrocarbonsat temperatures as low as ˜180 °C, much superior to the performance of traditional washcoated catalysts.

1. Introduction

Due to its excellent oxygen storage capacity and thermal stability, cerium oxide (ceria, CeO_2) has been an important material ingredient in various modern exhaust after-treatment devices such as three-way catalyst and diesel oxidation catalyst [1,2]. Beside this well-established application, ceria is also used as promising materials in gas sensor, water oxidation, water-gas-shift reaction, photo-catalysis, CO_2 reduction, and water purification [2–4]. As an important rare-earth oxide, ceria is consumed significantly, and there is an urgent need for developing strategies towards a sustainable and efficient utilization of ceria. In industry, the catalyst assembly processes such as pelletizing and washcoating are usually necessary to engineer the powder-form of ceria into practically functional ensembles. However, these traditional powder assembly and washcoating processes usually have several issues, such as significant pressure drop, compromised material usage efficiency, significant diffusion resistance, and lack of well-defined structural configurations [5–8]. For example, the washcoat process is widely used to fabricate automotive catalytic converters, where the ready-made catalyst powder (i.e., metal-oxide-supported noble metals) is uniformly coated on channeled honeycomb monoliths typically made of cordierite, a type of alumina magnesia silicate prototypically used in industry. A slurry consisting of active catalyst powders and additional binders is loaded to the monolith channel surfaces, forming a 20–200 μm thick catalyst layer via multiple repeated washcoating cycles. Such a thick layer of washcoat may cause large internal diffusion resistance directly impacting the device performance. Furthermore, it may also induce 20–30% pressure drop, leading to a significant energy and fuel penalty in automotive powertrain system.

Meanwhile, the recent development of monolithic catalysts integrating multi-functional nanostructures on two- or three-dimensional (2D or 3D) substrates provides a potential solution to solve the aforementioned challenges in the traditional powder-based catalyst processing. Especially for ceria, various nanostructures such as nanocrystals, nanoscale spherical/hollow structures, nanoporous structures, and hierarchical structures have been successfully synthesized and utilized in various applications [9]. Generally, the nanostructured ceria can offer attractive characteristics such as high surface areas, novel

* Corresponding authors.
E-mail addresses: cynam@bnl.gov (C.-Y. Nam), puxian.gao@uconn.edu (P.-X. Gao).

https://doi.org/10.1016/j.apcatb.2019.01.028
Received 14 June 2018; Received in revised form 27 December 2018; Accepted 9 January 2019
Available online 10 January 2019
0926-3373/ © 2019 Elsevier B.V. All rights reserved.

morphologies, tunable pore sizes, and adjustable surface chemistry, which can be beneficial for various catalytic actions. Moreover, the nanostructured ceria has been proved to be an near-perfect support for loading active metals with good dispersion, resulting in the enhanced catalytic performance, originating from the synergistic combination of metal and ceria [10–13].

Recently, several synthesis methods have been developed for the growing of various low-dimensional metal oxide nano-arrays on commercially available, 3D-channeled cordierite monolithic substrates [5,14–21]. Typical metal oxides such as ZnO, Co_3O_4, MnO_2 and TiO_2 could be grown on the 3D honeycomb cordierite in the form of nanorod or nanowire arrays, and the well-defined structural characteristics conveyed by these uniform nano-array catalysts could offer several advantages such as robustness, high material utilization efficiency, and improved catalytic activities, especially at low temperature [14,17,22–24]. Particularly, the synthesis of ceria nanotube arrays was successfully demonstrated on a 3D-channeled cordierite monolith by using the two-step ZnO nanostructure-array-template strategy [5,25]. Compared with other reported approaches based on the electrochemical deposition process which could integrate ceria nanostructures such as nanosheets and nanowires on a Cu foil [26,27], the process did not require a conductive substrate, and its process control was much simpler, making it suitable for the large-scale fabrication of ceria-nanostructure-array-based monolithic catalysts. Nevertheless, the further application of this type of ceria-nanostructure-based monolith is still challenging because of its low mechanical stability under the high space velocity and vibrational conditions [5].

On the other hand, due to the relatively low catalytic activity of ceria itself, it is necessary to combine ceria with noble metals to achieve desired catalytic performance. To this end, the development of deposition strategies for coating uniform nanoparticles with precise control of the catalyst loading and high material utilization efficiency is critical. Atomic layer deposition (ALD) is a well-established chemical vapor deposition technique capable of atomic-precision thickness control and uniform conformal coating [28–30]. Furthermore, ALD can be used to deposit noble metal nanoparticles suitable for various catalysis applications [31,32]. The self-limiting nature of the surface reactions during ALD process can be conveniently applied for depositing active species on the 3D parallel-channeled monolith integrated with array nanostructure, potentially enabling an excellent, catalytically activated device.

In this study, CeO_2-based composite nanoflake arrays were firstly successfully grown *in situ* on 3D-channeled cordierite honeycomb substrates using a simple but robust hydrothermal process involving only cerium precursor. This represents a unique one-step synthesis strategy that enables the integration of ceria nanostructures into nonconductive 3D cordierite honeycomb substrates suitable for practical applications, without requiring any foreign material additive or seeding layer. A self-seeding and etching-recrystallization process was used to explain the growth mechanism of CeO_2 nano-arrays on the cordierite channel surface based on the systematic structural investigation of time-dependent growth morphology. Moreover, ALD process was applied to incorporate uniformly-dispersed, size-controlled Pt nanoparticles on the surface of CeO_2 nanoflake nanostructures, which not only improved the material usage efficiency but also the uniformity of nanoparticle dispersion and size distribution. As a result, the obtained Pt/CeO_2 nano-array monolithic catalyst has displayed good catalytic oxidation activities over CO, hydrocarbons (C_3H_6 and C_3H_8), and NO at temperatures as low as 180 °C, with the corresponding conversion efficiency reaching over 90% despite the ~5-50 times lower material usage compared with the conventional wash-coated Pt catalyst. Especially, under the simulated exhaust condition of low-temperature diesel combustion (LTC-D) protocol developed by US DRIVE, the monolithic catalyst with low Pt loading (1 g/l) exhibited a good catalytic oxidation activity for CO and hydrocarbons with 90% conversion at temperatures as low as ~180 °C.

2. Experimental

2.1. Materials preparation

2.1.1. Growth of CeO_2 based nanoflake array device

The cerium precursor $Ce(NO_3)_2$•$6H_2O$ used in this study were purchased from Sigma-Aldrich without further purification. Cordierite honeycomb ceramic (mesh 600) was purchased from Corning Inc., which was washed with ethanol and water under an ultrasonic condition to remove residual contamination before the hydrothermal growth. Typically, 20 mM $Ce(NO_3)_2$·$6H_2O$ was dissolved in 40 ml water and then transferred into a Teflon-lined vessel with volume of 50 ml. A cordierite honeycomb substrate (1 cm × 2 cm × 3 cm, 600 cells per square inch, cpsi) was then immersed into the above precursor solution, and the hydrothermal reaction was carried out in a forced-air oven at 180 °C. The effect of different reaction time (4, 6, 12, 24, 48, and 72 h) was investigated. After the hydrothermal reaction, the substrate was carefully washed with water and ethanol and then dried at 90 °C for 12 h. Finally, all the prepared samples were annealed at 500 °C for 2 h under an ambient condition (ramp rate: 5 °C min^{-1}).

2.1.2. Deposition of Pt nanoparticles with ALD technique

ALD process was applied to deposit Pt nanoparticles on the as-synthesized CeO_2 nanoflake array structure integrated in the 3D cordierite honeycomb monolith. In the ALD process, trimethyl(methylcyclopentadienyl)platinum (IV) and O_2 were used as the Pt and oxygen precursors, respectively. The Pt precursor was heated to 70 °C to establish vapor pressure. The base pressure of ALD chamber was 0.4 Torr, and the Pt nanoparticle deposition was performed at 280 °C under 20 sccm nitrogen flow using a commercial ALD system (Cambridge Nanotech, Savannah S100). The Pt nanoparticle loading was controlled by adjusting the number of Pt ALD cycles (40 cycles). One ALD cycle consists of 1 s dosing of Pt precursor and 1 s dosing of O_2 into the ALD chamber, with the two precursor exposures separated by 30 s nitrogen purging. To look into the synergistic interaction between Pt and CSAO, control samples were fabricated using the same ALD process. The control substrates for Pt ALD include etched cordierite with a similar nanosheet array layer on the surface [23]; washcoated cordierite with Al_2O_3 with ~98 g/l loading; and washcoated cordierite with mixed Al_2O_3 of 81 g/l and CeO_2 of 8 g/L.

2.1.3. Preparation of conventional Pt/CeO_2-Al_2O_3 and Pt/Al_2O_3 wash-coat catalyst

A laboratory-prepared Pt/CeO_2 (5 wt.%) was mixed with Al_2O_3 powder (weight ratio 1:10), then dispersed into water with solid content of 20 wt.% for further washcoating process. Another coating slurry was made by dispersing commercial 1 wt.% Pt loaded Al_2O_3 powder (Alfa Aesar) into deionized water with a solid content of 20%. In a typical wash-coat process, the honeycomb cordierite substrate was first immersed into the slurry, taken out to blow away the residual slurry with forced air, and then heat-treated at 250 °C for 0.5 h. To achieve the identical Pt loading compared with the Pt/CeO_2 nano-array catalyst (1 g/l), the wash-coat process was repeated for several times. Finally, the wash-coated Pt/CeO_2-Al_2O_3 and Pt/Al_2O_3 catalysts were calcined at 500 °C for 2 h under ambient condition (ramp rate: 5 °C min^{-1}) for further characterization and usage.

2.1.4. Hydrothermal aging

To evaluate their hydrothermal stability during the LTC-D test, all monolithic catalysts were aged in a flow of 12%O_2, 6% CO_2, 6% H_2O in air at 700 °C for 120 h. The achieved catalysts were denoted as Pt(ALD)-CeO_2 array-HA, Pt/CeO_2-Al_2O_3 washcoat-HA and Pt/Al_2O_3 washcoat-HA, respectively.

2.1.5. Ultrasonic treatment

To check the mechanical stability of monolithic device, both Pt

(ALD)-CeO_2 array and Pt/CeO_2-Al_2O_3 washcoat catalysts were put in water and treated under ultrasonic condition for 30 min.

2.2. Materials characterization

The X-ray diffraction (XRD) patterns of the prepared catalyst monoliths were obtained by an X-ray diffractometer (D2 PHASER, BRUKER Corp.; scan range from 10° to 80° (2θ); Cu-Kα source). Scanning electron microscopy (SEM, Teneo LVSEM, FEI) and scanning transmission electron microscopy (STEM, Talos, FEI; 200 kV acceleration voltage) were used to characterize the structure and morphology of the prepared catalyst monoliths. The Pt nanoparticle size distribution was obtained by measuring the sizes of at least 300 individual Pt nanoparticles identified from STEM data. The loading amounts of Pt and CeO_2 were determined by the inductively coupled plasma (ICP) elemental analysis method. The N_2 adsorption-desorption testing was carried out by a surface analyzer (ASAP 2020, Micromeritics Corp.) to determine the surface area and pore size distribution according to the Brunauer-Emmett-Teller (BET) and Barrett-Joyner-Halenda (BJH) analyses. Before the measurements, a degassing process was performed at 150 °C for 6 h.

2.3. Catalytic performance test

2.3.1. Single hydrocarbon oxidation

Propylene and propane were selected for the hydrocarbon oxidation reaction. Such hydrocarbons are generated from the combustion of liquid fossil fuels and can contribute to the formation of photochemical smog and ozone pollution. It still remains as a great challenge to remove these pollutants completely, especially at low temperature even with the deployment of emission controlling systems such as diesel oxidation catalyst (DOC). An automated microreactor (BenchCAT, Altamira Instruments) was used to test the oxidation reactions of these hydrocarbons by the prepared catalyst monoliths, with the inlet and outlet gas species detected by a gas chromatography system (Agilent Micro-GC) equipped with two columns and two thermal conductivity detectors. The reactant gas was mixed with 20 ml min^{-1} 5% C_3H_6, 20 ml min^{-1} 3% C_3H_8, 20 ml min^{-1} O_2 and 140 ml min^{-1} N_2 (0.5% C_3H_6, 0.3% C_3H_8, 10% O_2 and 89.2% N_2) with a total flow rate of 200 ml min^{-1}. One piece of monolithic honeycomb catalyst (25 channel, 0.5 cm × 0.5 cm × 1 cm, 0.25 ml) was wrapped with a catalyst cushion mat and then loaded into the center of quartz tube (1 in. diameter). A thermocouple wire was inserted into the reactor for measuring the catalyst bed temperature. With this set up, the space velocity could be controlled at 48,000 h^{-1}. Considering the total weight/volume of monolithic nanorray catalyst honeycomb (0.1 g/0.25 ml) and the catalyst loading ratio (~5 wt.%), the actual catalytic material used in the test was only 5 mg.

2.3.2. Single CO and NO oxidations

CO and NO are also important pollutants from automotive engine, which have a significant impact on the environment and human health. NO oxidation is one of the main tasks of DOC to increase the NO_2/NO_x ratio in order to improve the NO_x reduction performance of the downstream selective catalyst reduction (SCR) unit. The performance of CO and NO oxidations by the prepared catalyst monoliths was evaluated in a horizontal quartz tube reactor, heated by a tube furnace (Fisher Scientific). The catalyst loading condition is similar to what was used in the hydrocarbon oxidation test. Each experiment was initiated by a temperature ramp (ramp rate: 5 °C min^{-1}; temperature recorded by a temperature logger (Omega)). The CO oxidation test was performed under a gas mixture consisting of 1% CO, 10% O_2, and Ar balance, and the NO oxidation test under a gas mixture of 0.02% NO, 8% O_2, and N_2 balance. The total gas flow rate was set to be 200 ml min^{-1} to maintain 48,000 h^{-1} space velocity (SV). The conversion efficiency of CO oxidation is calculated based on the CO_2 concentration that is detected by a residual gas analyzer (RGA 200, Stanford Research Systems). Fourier transform infrared spectrometer (FTIR, Thermo-fisher Nicolet 6700) was calibrated for NO and used for on-line gas analysis. TQ Analyst software and partial least squares (PLS) method were used for the calibration.

2.3.3. Simulated LTC-D gas testing

The simulated diesel exhaust oxidation activities of catalysts were evaluated by following the protocol developed by the Advanced Combustion and Emission Control (ACEC) Technical Team of U.S. DRIVE. A self-designed plug-flow reactor system was applied to measure the simulated exhaust light-off. The monolithic catalysts were cut wrapped with 3 M Mat-Mount and loaded into a quartz tube. A thermocouple was placed approximately at 0.2 cm from the catalyst front to measure the inlet temperature. Space velocity was kept at 60,000 h^{-1} throughout all tests. With the U.S. DRIVE protocol, the composition of the "LTC-D" simulated exhaust is [O_2] = 12%, [H_2O] = 6%, [CO_2] = 6%, [H_2] = 400 ppm, [CO] = 2000 ppm, [NO] = 100 ppm, [C_2H_4] = 833.5 ppm, [C_3H_6] = 333 ppm, [C_3H_8] = 111 ppm, and N_2 balance. The water vapor was introduced via a water pump and heated tubing lines held at 120 °C. The concentrations of CO and hydrocarbons were measured via a customized Agilent GC–MS with mass spectrum detector and thermal conductive detector. The testing was finished through a ramping process from 100 °C to 600 °C with a rate of 2 °C/min.

3. Results and discussion

3.1. Growth of CeO_2 nanostructures

The hydrothermal growth provides a simple and robust synthetic protocol, where $Ce(NO_3)_3$ could be used as a cerium source without requiring any additives for the growth of ceria nanostructures. During the growth process, the hydrolysis of cerium ions was forced to take place slowly under the reaction temperature. To elucidate the ceria nanostructure array formation mechanism on the cordierite honeycomb monolith, a series of time-dependent experiments were carried out, and the morphological evolution of ceria nanostructures were identified with respect to the reaction time (Fig. 1). After 4 h of reaction, only surface became rough due to the formation of some ceria nanoparticles on the channel surface of 3D honeycomb cordierite (Fig. 1a). Some nanoflake clusters began to grow on top of the nanoparticle layer after 6 h (Fig. 1b), and there was a more visible growth of nanoflakes when the reaction time was extended to 12 h (Fig. 1c). After 24 h of growth, the surface coverage of nanoflakes became more uniform, generating an array morphology (Fig. 1d). If the reaction time was further increased beyond 24 h, the formation of larger micrometer-scale spherical particles can be observed on both the surface of nanoflake arrays and in the inner space of nano-array (Figs. 1e and f). From the ceria loading ratio on the cordierite substrate (determined by the ICP method) with respect to varying total reaction time, it can be found that generally the nanoflake growth was fast within the first 24 h of reaction but was slowing down after 24 h (Figure S4 and Table S2).

The nanoflake array sample obtained from the 24-hour total reaction time was further characterized by STEM (Fig. 2). From the high-angle annular dark field (HAADF) image (Fig. 2a), numerous white dots appeared onto the flake-like nanostructure, which can be ascribed the cerium with heavier atomic mass. According to the elemental mapping results (Figs. 2b-f) obtained by the energy dispersive spectroscopy (EDS), the nanoflake structure is found to be mainly consisting of Al (23.0 wt.%), Si (15.7 wt.%), Ce (25.2 wt.%) and O (36.1 wt.%) while no observed presence of Mg. Considering the reactants composed only cerium nitrate, water and cordierite substrate made of magnesium aluminum silicate, the elements Al and Si on nanosheet can only be contributed to the partial dissolution of cordierite surface then recrystallization (re-incorporation) of the dissolved elements during the

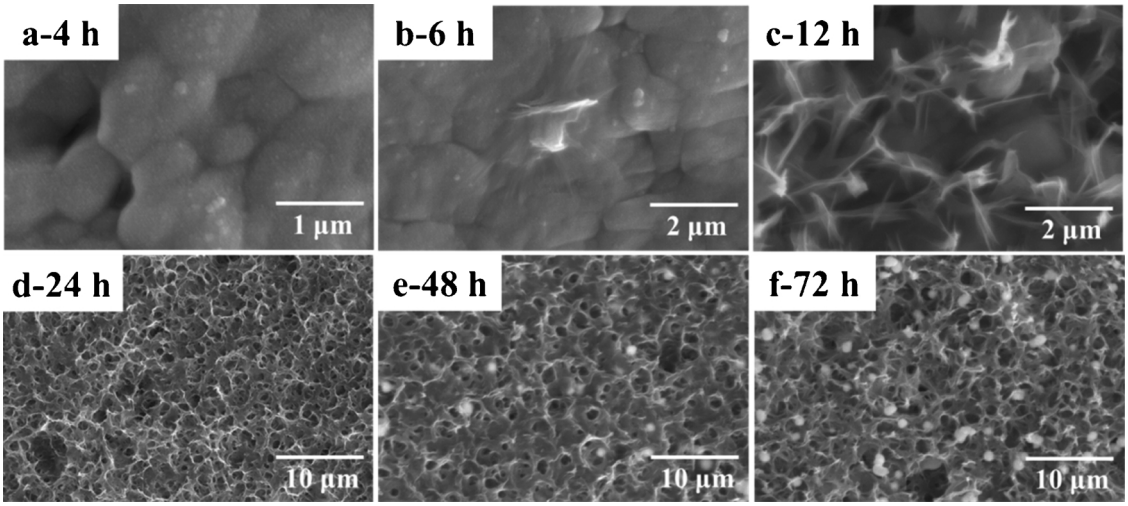

Fig. 1. Top-view SEM images of CeO_2 nanostructures on the 3D-channeled cordierite honeycomb grown for different total reaction times.

hydrothermal reaction. As shown in Figure S1, the mixing of nanoflake (light black) and broken cordierite parts (deep black) can be found in the HADDF image at lower magnification. The difference of new generated nanoflake and original cordierite can be identified by the existence of cerium and magnesium, respectively. Moreover, some dense parts corresponding to cerium can also be observed from Figure S1e, which are tightly attached on the original cordierite surface.

Figs. 3b and c show the high-resolution SEM images of flake nano-array, where each unit nanoflake has a thickness of approximately several nanometers. From the cross-sectional SEM (Fig. 3c), two distinctive layers can be identified in the grown ceria nano-array film, including the dense bottom ceria nanoparticle aggregation layer and the top nanoflake array layer, with the total flake nano-array film thickness of ~2 μm. High-resolution TEM (HRTEM) reveals that the thickness of the dense bottom layer is ~100 nm, and it has a polycrystalline structure consisting of numerous aggregated ceria nanoparticles in the size of several nanometers (Figs. 3d-f). The lattice fringes, clearly observed in HRTEM, has a spacing of 0.31 nm, matching the (111) crystal plane of fluorite CeO_2 (Fig. 3i). The nanoflakes are rooted into the dense polycrystalline layer, suggesting that the dense bottom nanoparticles layer served a seeding layer, assisting the growth of flake-like nanostructure with increasing total reaction time. A typical individual CeO_2 nanoflake inspected in HRTEM clearly demonstrates an irregular porous structure with pore sizes of 3–20 nm (Figs. 3g-i). A

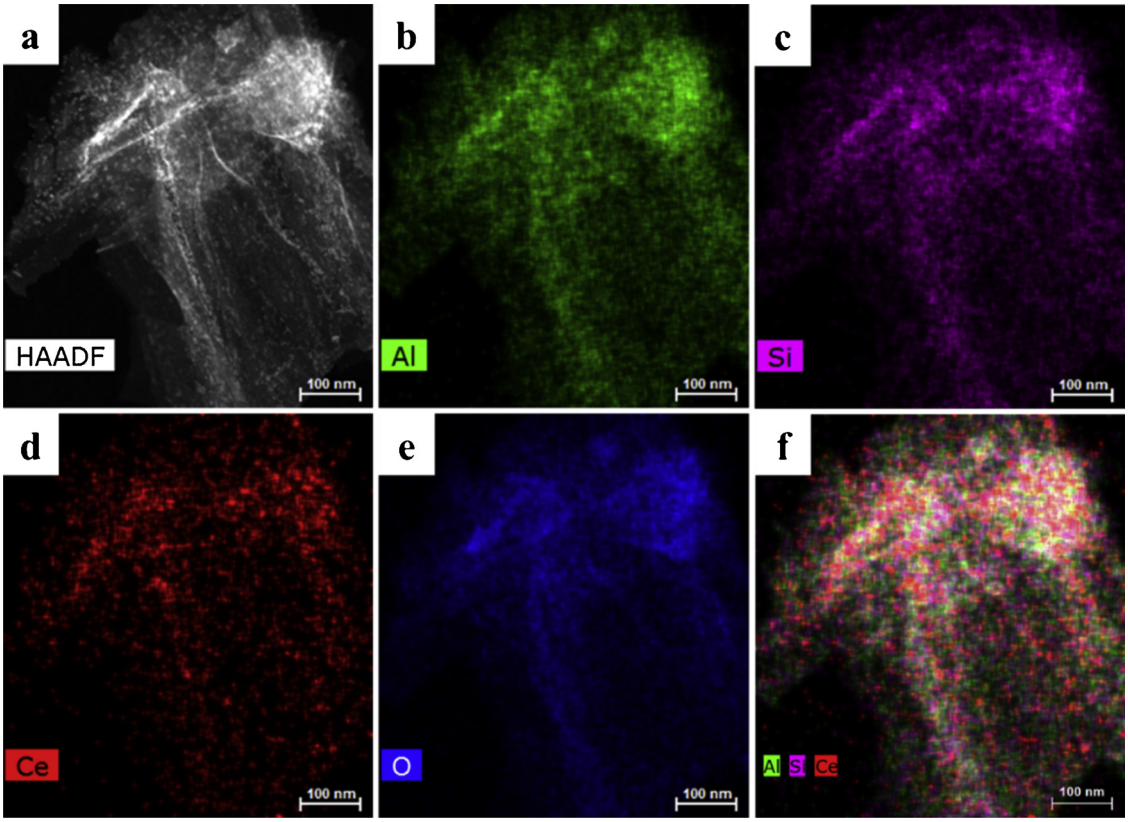

Fig. 2. (a)HADDF-STEM image of the Ce-Si-Al-O (CSAO) nanoflake; (b–f) corresponding EDS elemental mapping of Al, Si, Ce, O and Al-Si-Ce mixed recorded for the area shown in figure (a).

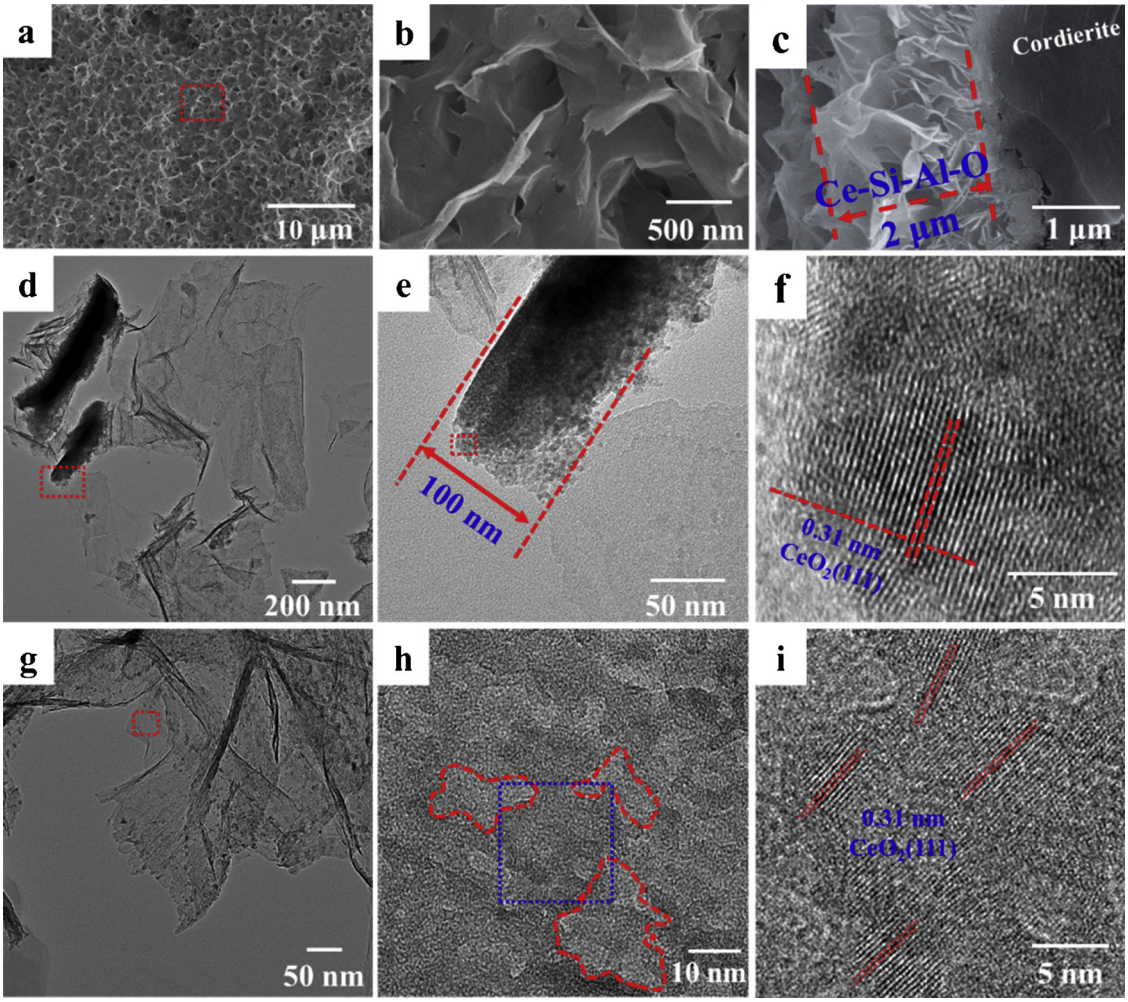

Fig. 3. SEM (a and b, top-view; c, cross-section) and TEM (d–i) images of CSAO nano-array structures obtained after 24-hour hydrothermal growth reaction.

further analysis of selected area from the nanoflake confirms the same lattice spacing of 0.31 nm corresponding to (111) plane of fluorite CeO_2 as observed in the dense bottom nanoparticle layer (Fig. 3f), which demonstrates the ceria nanoparticles were successfully incorporated into the nanoflake to form the Ce-Si-Al-O (CSAO) mixed oxide. From the BET analysis (Figure S3), the surface area of as-synthesized CSAO nano-array monolith could be up to 15.1 $m^2 g^{-1}$, which was much higher than that of the blank cordierite honeycomb (< 0.5 $m^2 g^{-1}$). The average pore size of nanoflakes was ca. 10 nm, consistent with the TEM results.

Based on the observed time-dependent growth structure evolution, a formation process could be proposed, including in-situ-dissolution, self-seeded nucleation and in-situ-recrystallization-growth processes of CeO_2-based CSAO nanoflakes (Fig. 4). Starting from the smooth surface of 3D-channeled cordierite, when the hydrothermal reaction is carried out at 180 °C, the surface cordierite ($(2MgO{\cdot}2Al_2O_3{\cdot}5SiO_2)$) was firstly slowly etched in appropriate cerium nitrate solution. Meanwhile, it is generally expected that the oxidation of cerium ions starts via the hydrolyzation reactions: $Ce^{3+} + OH^- + H_2O + O_2 \rightarrow Ce(H_2O)_x(OH\text{-})_y^{(4-x)+}$; $Ce(H_2O)_x(OH\text{-})_y^{(4-x)+} + H_2O \rightarrow CeO_2{\cdot}2nH_2O + H_3O^+$, as they have been reported for the formation of CeO_2 nanocrystals [33,34]. One major difference in this growth process was the absence of any additives, which results in a much slower reaction rate as well as different growth morphologies. For instance, the growth process does not yield any appreciable formation of ceria powder even after 72 h of growth reaction; the growth solution remains relatively transparent while there is a visible deposition of a yellow thin film layer only on the internal wall of Teflon reactor and the growth substrate (pictures not shown). Combined with the discussed analysis of ceria nanostructure on the cordierite surface, it can be inferred that the nucleation of CeO_2 nanocrystals was taking place primarily on the solid-liquid interface through a heterogeneous nucleation. It is suggested that the growth reaction mainly relying on such a heterogeneous nucleation prevented the uncontrolled nucleation and growth of micrometer-sized ceria structures and greatly helped the preferred growth of ceria nanostructures on the surface of 3D-channeled honeycomb cordierite ultimately. Specifically, with the reaction further proceeding, the surface of cordierite is covered with a thin layer of an agglomerated ensemble of ceria nanoparticles, and this thin layer might also prevent the cordierite surface from further etching. With the growth of this layer, the dissolved Al and Si species began to recrystallize/re-incorporate to form CSAO nanoflakes (self-seeding) which was also driven by the change of solution acidity due to the crystallization of CeO_2 nanoparticles. As the hydrothermal growth further progresses, the density of grown nanoflakes increases, eventually forming the nanoflake array structure as observed. The micrometer-sized spherical ceria particles that started appearing after 48 h of growth reaction indicates that the further growth of nanoflakes became limited once the total reaction time is prolonged over 24 h, which is consistent with the small change of ceria loading ratio on the cordierite substrate after the 24 h of hydrothermal reaction (Figure S4 and Table S1). The limited growth of CSAO nanoflakes may be due to the restricted amount of etched cordierite and therefore, insufficient amounts of dissolved Al and Si species for supporting the further growth. This may also explain the formation of

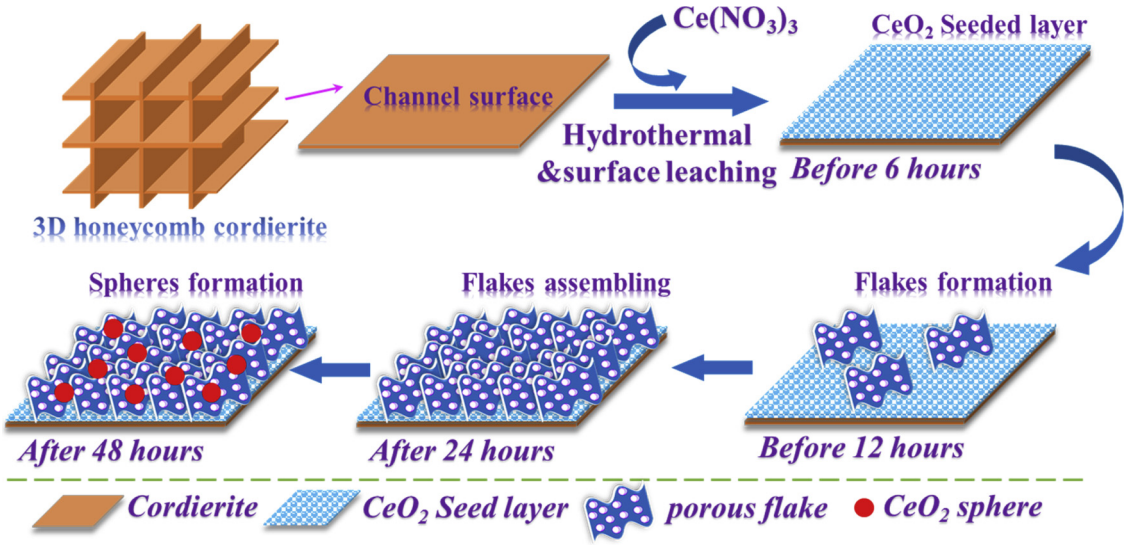

Fig. 4. Schematic illustration of the structural evolution of CSAO nanoflake arrays during the hydrothermal growth process.

sphere-like ceria structures among CSAO nanoflakes.

3.2. Decoration of Pt nanoparticles by ALD

As an efficient, conformal thin film growth technique, the ALD process employs the self-limiting chemical reactions between gaseous metal-organic precursors and the solid surface of target substrates, which generally allows a precise, atomic-scale control of deposited material thickness [28]. For the deposition of noble metals, ALD often results in the formation of nanometer-sized spherical particles when the number of ALD cycles is small [31,35]. This ability to deposit metal nanoparticles in vapor phase finds useful applications in generating well-controlled size and distribution of noble metal catalyst nanoparticles on various metal oxide supports such as SiO_2, TiO_2, Al_2O_3 and $SrTiO_3$ [31,36–39]. Alternative to the conventional solution-based metal particle loading methods such as washcoat process, the capability of ALD to create well-dispersed, size-controlled metal nanoparticles on metal oxide surface potentially provides a promising method of fabricating advanced catalyst materials with a greatly improved material usage efficiency. However, it is not trivial to apply the ALD process to loose metal oxide powder materials typically utilized in the catalyst community because the vapor-phase ALD precursor mass diffusion into the bulk of powder materials is difficult during the typical ALD process. This CSAO nanoflake array structure integrated on the 3D-channeled honeycomb substrate here could resolve this mass diffusion issue during the ALD process as a result of the open, penetrable 3D channels in the cordierite honeycomb and the ceria-based nanostructure with numerous macropores on the surface that can be directly exposed to the ALD precursors. Indeed, the ALD process enables a formation of well-dispersed Pt nanoparticles with ~3.8 nm diameter on the surface of CSAO nanoflake arrays, ultimately contributing to a significantly enhanced catalytic performance of Pt/CSAO nanoflake array monoliths compared with both the conventional washcoated Pt/CeO_2-Al_2O_3 and Pt/Al_2O_3 counterpart.

Figs. 5a-c show TEM images of typical CSAO nanoflakes after Pt nanoparticle deposition by the ALD process. It is clearly observed that the Pt nanoparticles are well dispersed onto the surface of CSAO nanoflake structures. By measuring the particle size distribution (Fig. 5d), the average Pt nanoparticle size was ca. 3.77 nm (± 0.06 nm). The high-resolution lattice image obtained from the Pt nanoparticle (Fig. 5c) reveals 0.23 nm lattice spacing, which matches the {111} planes of Pt and is consistent with what was reported for the ALD-prepared Pt nanoparticle on $SrTiO_3$ surface [37]. The Pt nanoparticles not only have high crystallinity with clearly resolved crystal facets but also are spatially well-dispersed on the surface of CSAO nanostructures. This observed uniformity of Pt nanoparticle deposition reveals the advantage of monolithic 3D-channeled cordierite substrates over the conventional powder form of metal oxide supports, wherein the continued ALD cycles typically resulted in a much less uniform Pt nanoparticle deposition due to the clogged inner pores of metal oxide powder supports with increasing number of ALD cycles [31]. There is virtually no loss of surface area or change in pore size in the synthesized monolithic Pt/CSAO nano-array catalyst integrated in the 3D cordierite honeycomb after the Pt nanoparticle deposition by the ALD process (as shown in Figure S3), highlighting that the combination of the new self-seeded hydrothermal growth scheme of ceria-based nanostructure, the 3D-channeled cordierite monolith substrate, and the uniformly controlled deposition of Pt nanoparticles by the ALD process demonstrates an unique fabrication methodology that enables a noble-metal/CSAO nano-array monolith catalyst having well-controlled nanostructures that result in a good catalytic performance as shown next.

3.3. Catalytic oxidation of single hydrocarbons, CO, and NO

The enhanced catalytic performance of monolithic $Pt(ALD)/CeO_2$ nano-array catalysts can be confirmed by testing the catalytic oxidation of hydrocarbons, CO, and NO. The performance of monolithic ALD-Pt/CSAO nano-array catalysts was compared with that of the conventional wash-coated Pt/CeO_2-Al_2O_3 and Pt/γ-Al_2O_3 catalyst with the same Pt loading (1 g/l), which required a ~5 μm thick wash-coat layer (Figures S4 and S5). Figs. 6a and b illustrate the temperature-dependent conversion of propylene and propane oxidation for the monolithic Pt (ALD)/CSAO nano-array catalyst and the control Pt/CeO_2-Al_2O_3 and Pt/Al_2O_3 wash-coat catalyst. For the propylene oxidation, the light-off curves obtained from both samples were sharp, indicting a fast conversion with increasing reaction temperature. The 90% oxidation conversion temperature (T_{90}) of monolithic Pt(ALD)/CSAO nano-array catalyst for the propylene oxidation is ca. 180 °C, ~40 and 90 °C lower than that of the wash-coat counterpart, as listed in Table 1. The T_{90} of propane oxidation was achieved at 180 °C by the ALD-Pt/CSAO nano-array catalyst while only 40% conversion was observed at 500 °C over the Pt/Al_2O_3 wash-coat catalyst. As shown in Fig. 6c, the complete CO oxidation can be achieved above 185 °C on the Pt(ALD)/CSAO nano-array catalyst which is similar to Pt/CeO_2-Al_2O_3 wash-coat catalyst, while the temperature for a similar conversion needs to be ~238 °C over the Pt/Al_2O_3 wash-coat catalyst.

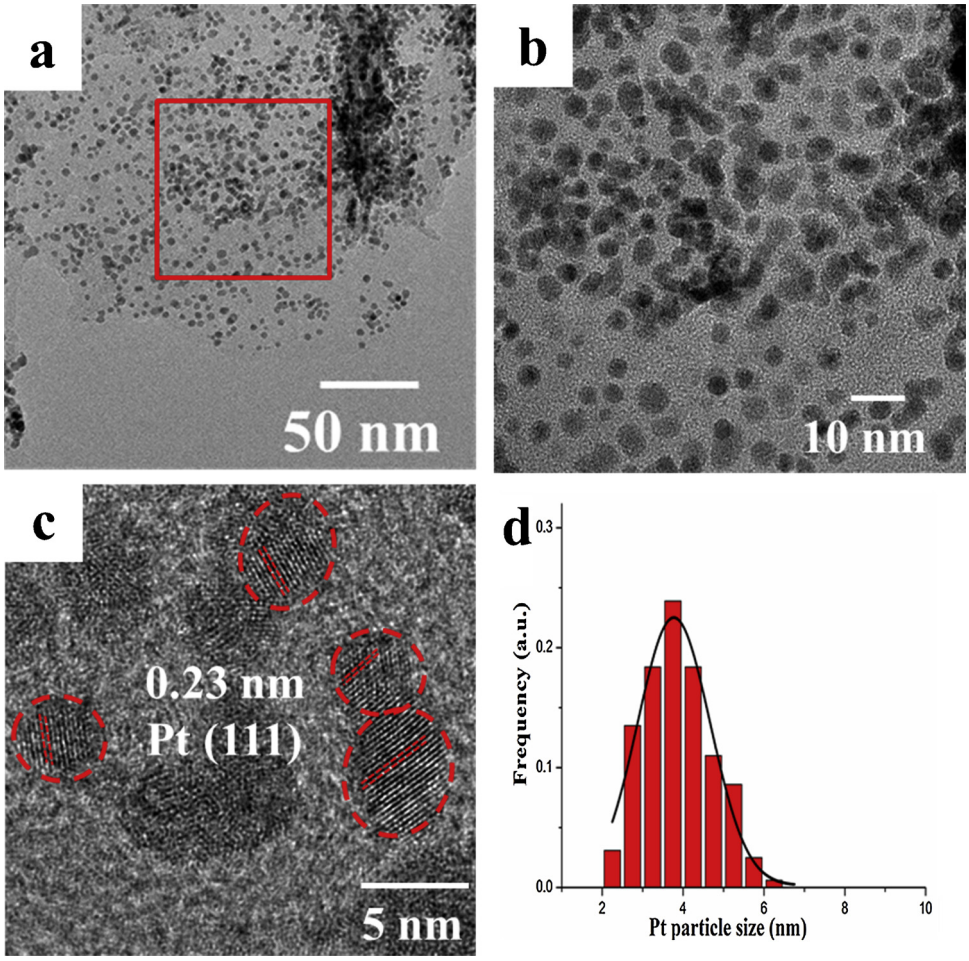

Fig. 5. TEM images (a, b and c) of Pt nanoparticles, and (d) size distribution of CSAO/Pt nanoflake array integrated on a cordierite honeycomb monolith.

Moreover, an even better low-temperature catalytic performance of Pt(ALD)/CSAO nano-array catalyst for the NO oxidation was observed, nearly achieving the thermodynamic performance limit dictated by the NO oxidation reaction equilibrium (blue line in Fig. 6d) which was calculated by the Aspen Plus software. In a typical catalytic NO oxidation, achieving a high conversion efficiency approaching the thermodynamic limit is extremely difficult, especially at low temperature due to the reaction kinetic limitation [40–42], as clearly exemplified from the tested control Pt/CeO_2-Al_2O_3 and Pt/Al_2O_3 washcoat catalyst (Fig. 6d). Clearly, in the case of this monolithic ALD-Pt/CSAO nano-array catalyst, a ~95% NO-NO_2 conversion efficiency could be obtained below 200 °C, which is in a stark contrast with the only ~67% maximum conversion efficiency achievable in the Pt/Al_2O_3 wash-coat catalyst at a much higher temperature, 327 °C. The previously reported Pt-based oxidation catalysts in literatures were surveyed and listed in Table 2. The catalytic oxidation activities are clearly promoted significantly in hydrocarbons, CO, and especially NO at low temperature over the monolithic Pt(ALD)/CSAO nano-array catalyst. The material usage, including both Pt and ceria, is ~5-50 times lower in monolithic Pt(ALD)/CSAO nano-array catalyst.

The enhanced performance of monolithic Pt(ALD)/CSAO nano-array catalyst integrated on the 3D-channeled cordierite honeycomb can be understood primarily by the improved mass transport that the open, hierarchical nano-array structure allows. In the case of wash-coat catalysts, the catalyst coating layer with a much larger thickness (40–100 μm) and material amounts is required for achieving a targeted catalytic performance [43,44], which not only limits the mass transport into the densely coated layer but also severely compromises the material utilization efficiency. Even if more porous metal oxide supports are used (e.g., Al_2O_3 and TiO_2) in the wash-coat slurry, the mass transport is still less than ideal due to the inevitable mass diffusion problem especially in a challenging environment (high space velocity) which typically exists in the automotive emission exhaust [45–48]. To estimate the influence of diffusion on reaction rates, the Weisz–Prater criterion ($N_{W\text{-}P}$) of wash-coat sample have been calculated based on other studies [48,49] as shown in Table S1 in the SI. In term of CO oxidation, the $N_{W\text{-}P}$ is about 14.77 at 500 K with an average waschoat thickness of 50 μm. Here, the developed monolithic Pt(ALD)/CSAO nano-array catalyst is expected to have a significantly improved mass diffusion to the catalytically active sites existing inside the catalyst layer because of the open space (20–500 nm) that provides an ideal environment for an efficient internal mass diffusion. Given that the thickness of the active Pt/CSAO nano-array is only ~2 μm, compared with the 50 μm thickness of the traditional wash-coat catalyst layer (Figure S11), the $N_{W\text{-}P}$ of nano-array is only 0.023 assuming that the effective diffusivity of nano-array is the same as the wash-coat catalyst. With a much lower Weisz–Prater criterion number than that of wash-coat catalysts, the array nanostructured catalyst clearly has a much smaller limitation in mass transfer than washcoat catalysts, further ensuring that reactant and product molecules can efficiently reach and leave the active catalyst sites.

Another important factor that should have contributed to the enhanced catalytic performance of Pt(ALD)/CSAO nano-array catalyst is the strong, catalytically synergistic interaction of Pt and CSAO augmented by the uniform spatial distribution of size-controlled Pt nanoparticles on the CeO_2 based CSAO nanoflakes achieved by the ALD process. The Pt-CeO_2 heterogeneous catalyst system has been widely studied and proven to be very efficient for numerous reactions

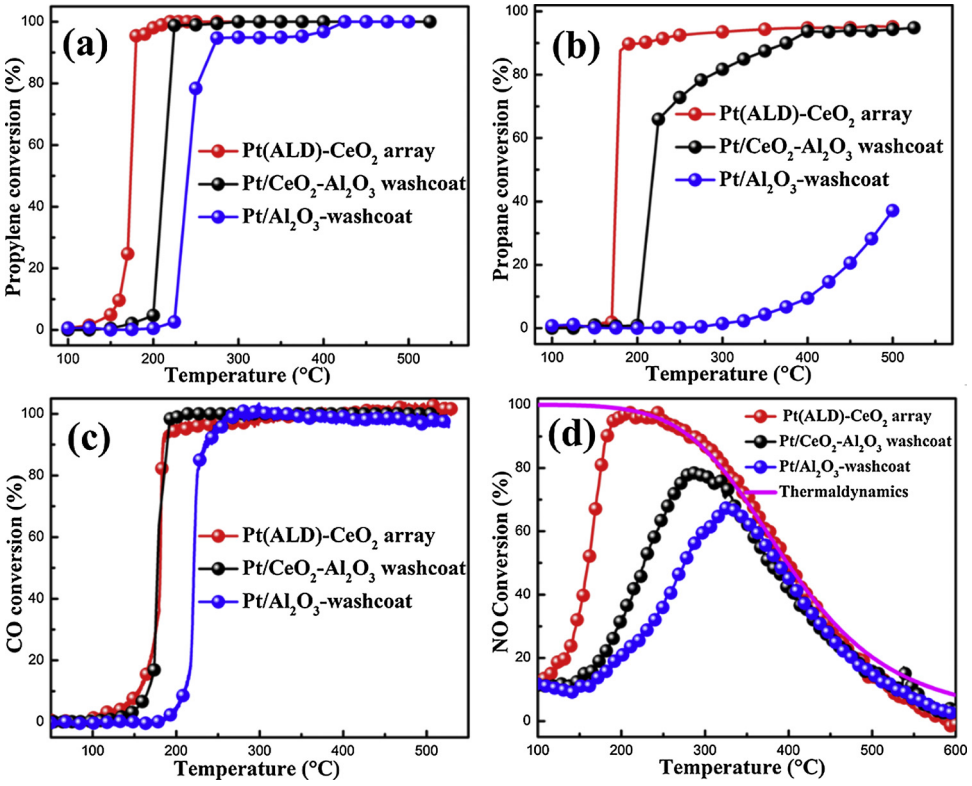

Fig. 6. Temperature dependent catalytic oxidation conversions of (a) propylene, (b) propane, (c) CO, and (d) NO over Pt(ALD)/CeO_2 nano-array, washcoated Pt/CeO_2-Al_2O_3 and Pt/Al_2O_3 monolithic catalysts.

including CO oxidation, hydrocarbon combustion, water-gas-shift reaction, and steam reforming reactions [50–54]. Generally, the synergistic catalytic effect is expected to increase as the interfacial area between Pt nanoparticles and the ceria support increases. In the synthesized Pt(ALD)/CSAO nanoarray catalyst, the active Pt nanoparticles were uniformly anchored without any substantial spatial overlapping or agglomeration on each CSAO nanostructure unit by the ALD process, providing an abundant Pt-CeO_2 interface area available for the catalytic oxidation reactions. With the assistance of the open nanoflake array geometry that has a large surface area per volume (as confirmed by the BET analysis), most of the Pt nanoparticles and Pt-CeO_2 interfaces can be fully exposed to the reactant molecules to undergo the catalytic oxidation. For the washcoated Pt/Al_2O_3, the oxidation activities are much lower especially for propane and NO despite the similar Pt loading, further demonstrating the synergistic catalytic effect originating from the Pt-Ce interaction [55,56]. More control samples were further studied to understand the importance of Pt-Ce interaction as shown in the following simulated gas testing results.

3.4. DOC performance in simulated LTC-D exhaust

Figs. 7a-c show the CO and hydrocarbons light-off curves for the Pt(ALD)/CeO_2 nano-array, washcoated Pt/CeO_2-Al_2O_3, and Pt/Al_2O_3 monolithic catalysts. Over the Pt(ALD)/CeO_2 nano-array monolithic catalyst, the light-off temperature (temperature of 90% conversion, T_{90}) of CO, C_2H_4, C_3H_6 and total hydrocarbon (THC) are all around 180 °C at which most catalyst systems in today's vehicles are ineffective. With the same Pt loading, the light-off temperatures for THC of washcoated Pt/CeO_2-Al_2O_3 and Pt/Al_2O_3 monolithic catalysts are 56 °C and 67 °C higher than that of Pt(ALD)/CeO_2 nano-array monolithic catalyst as displayed in Fig. 7d. Compared to CeO_2-free catalyst, the catalysts with CeO_2 exhibited much better activities in CO and HC oxidations. Over these three catalysts, CO oxidation always takes place first, and then both ethylene and propylene oxidation occur almost simultaneously. In this simulated LTC-D exhaust, propane is the most difficult hydrocarbon to be oxidized, especially at low concentration. Nevertheless, propane constitutes only a minor fraction of the total hydrocarbons, thus keeping the light-off temperature of THC at a lower level. Moreover, during 3 cycles of tests (ramp up-ramp down) as shown in Figure S8, the light-off curves over the Pt(ALD)/CeO_2 nano-array monolithic catalyst overlap with little change, suggesting its good stability and repeatable activities.

To confirm the important role of the nanoarray structure and the synergistic interaction between Pt and CeO_2, a series of control samples

Table 1
A comparative summary of catalytic oxidation activities and structural properties of Pt/CeO_2 nano-array, washcoated Pt/CeO_2-Al_2O_3 and Pt/Al_2O_3 monolithic catalysts.

catalysts	C_3H_6-T_{90} (°C)	C_3H_8-T_{90} (°C)	CO-T_{90} (°C)	NO-T_{max} (°C)	Surface area ($m^2\,g^{-1}$)	Pore diameter (nm)
Pt(ALD)/CSAO	**180**	**180**	**185**	**183(90%)**	8.5	9.9
1%Pt/CeO_2-Al_2O_3 washcoat	**224**	**382**	**189**	**286(79%)**	48.1	8.2
1%Pt/Al_2O_3 washcoat	**270**	**> 500**	**238**	**327(67%)**	52.0	7.9

Table 2
A comparative structural and performance characteristic summary of Pt based oxidation catalysts over propylene, propane, CO, and NO in literature under dry condition as compared to the current work. (:P: powder; M: monolith.).

	Catalysts	Form	catalyst usage	Pt usage	Gas con.	T_{90} (°C)	Reaction rate at 200 °C (mol g_{cat}^{-1} s^{-1})	Ref.
C_3H_6								
	Pt-K_2O/Al_2O_3	P	150 mg	6 mg	0.7%	260	3.47×10^{-5}	[57]
	Pt/ZrO_2	P	50 mg	0.25 mg	1.0%	200	1.49×10^{-5}	[58]
	Pt/Al_2O_3	P	30 mg	0.03 mg	0.06%	180	7.44×10^{-7}	[59]
	$Pt/Ce_{0.68}Zr_{0.32}O_2$	M	N/A	N/A	0.09%	300	N/A	[60]
	Pt/CSAO	**M**	**5 mg**	**0.25 mg**	**0.5%**	**180**	**14.6×10^{-5}**	**This work**
C_3H_8								
	$Pt/SrTiO_3$	P	N/A	N/A	0.25%	250	–	[37]
	Pt/Al_2O_3	P	200 mg	2 mg	2.5%	240	0.35×10^{-5}	[61]
	Pt/Al_2O_3	M	250 mg	0.5 mg	0.1%	> 450	0	[62]
	Pt/CSAO	**M**	**5 mg**	**0.25 mg**	**0.3%**	**180**	**8.03×10^{-5}**	**This work**
CO								
	Pt/Al_2O_3	M	250 mg	0.5 mg	0.1%	159	5.95×10^{-6}	[62]
	Pt/Al_2O_3	M	300 mg	6 mg	1.0%	235	1.24×10^{-6}	[63]
	Pt/CeO_2	P	50 mg	0.5 mg	5%	220	1.67×10^{-5}	[64]
	Pt/CSAO	**M**	**5 mg**	**0.25 mg**	**0.5%**	**185**	**2.97×10^{-4}**	**This work**
NO								
	Pt/Al_2O_3	P	100 mg	1.5 mg	0.05%	250	**1.34×10^{-7}**	[65]
	Pt/Al_2O_3	P	50 mg	2.4 mg	0.1%	320	**4.46×10^{-7}**	[66]
	Pt/Al_2O_3	M	N/A	N/A	0.05%	270	N/A	[67]
	Pt/CSAO	**M**	**5 mg**	**0.25 mg**	**0.02%**	**183**	**5.95×10^{-6}**	**This work**

from the same ALD process were fabricated for a detailed comparison, i.e., etched cordierite with a similar nanosheet array layer on the surface; washcoated cordierite with Al_2O_3; washcoated cordierite with mixed Al_2O_3 and CeO_2. As shown in Figures S9 a and b, with the same nanosheet array structure, the CeO_2 based nanoarray system exhibited a much higher activity than that of nanosheet array with etching cordierite in which the nanosheet unit is of similar composition to the cordierite, indicating the crucial importance of the existing CeO_2 and Pt-CeO_2 interaction. For washcoat samples (Figures S9 c and d), their activities are lower than that of CeO_2 based nanoarray catalyst despite the same ALD process used. The better mass transfer or lower diffusion resistance in nanosheet array structure with populated pores might be one of the reasons to lead to a better DOC performance in CeO_2 nanoarray system. After the hydrothermal aging, the measured light-off temperatures of washcoat catalysts increase compared with those of the nano-array catalyst, as shown in Fig. 8. For the Pt(ALD)/CeO_2 nanoarray after hydrothermal aging, the light-off temperature (T_{90}) of CO, C_2H_4, C_3H_6 and total hydrocarbon (THC) are 220 °C, 272 °C, 272 °C and

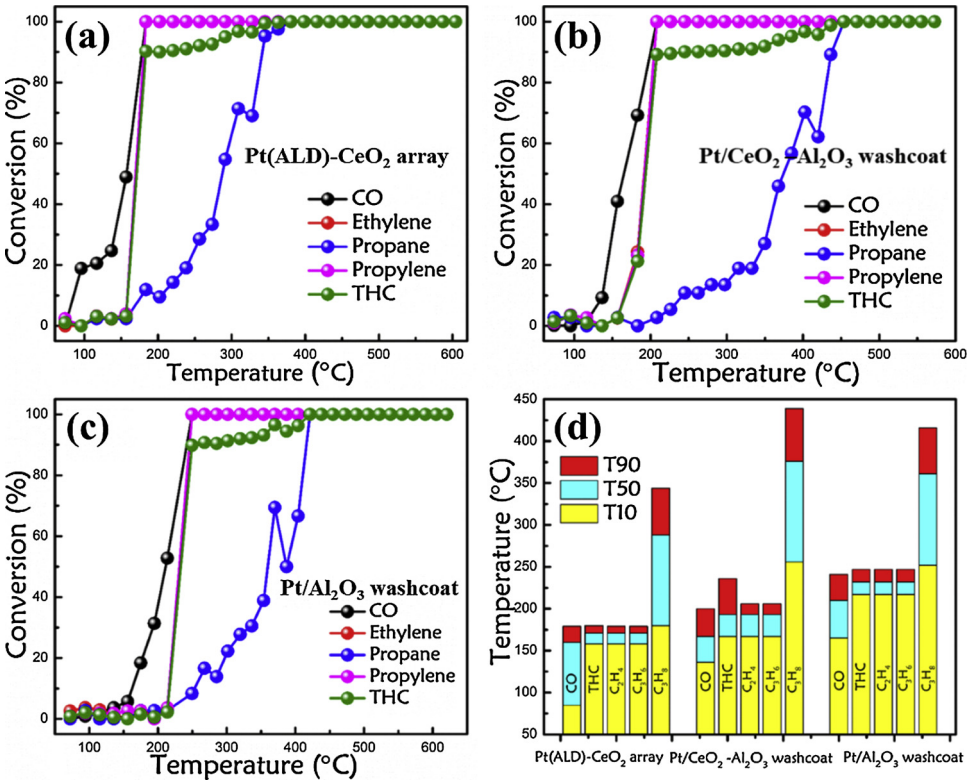

Fig. 7. DOC activity in the LTC-D simulated exhaust of (a) Pt/CeO_2 nano-array, (b) washcoated Pt/CeO_2-Al_2O_3 and (c)Pt/Al_2O_3 monolithic catalysts. (d) Comparison of T10, T50 and T90 (temperature of 10, 50 and 90% conversion) over the three DOC catalysts. The Pt loading on all catalysts is 1 g/L.

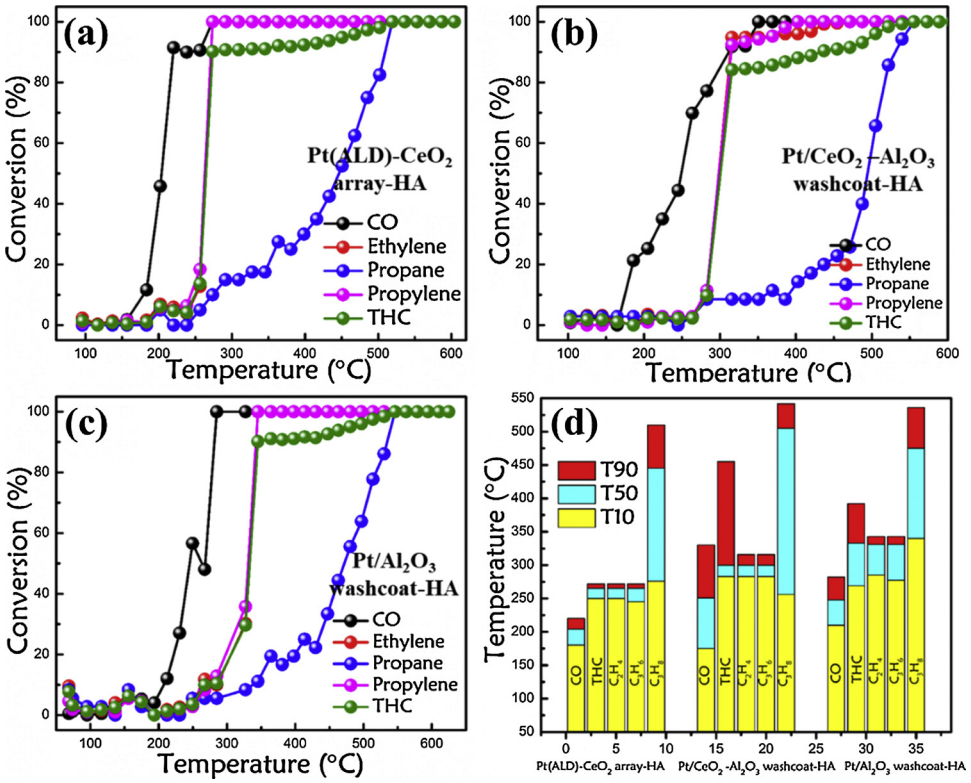

Fig. 8. DOC activity in the LTC-D simulated exhaust of (a) Pt/CeO_2 nano-array, (b) wash-coated Pt/CeO_2-Al_2O_3 and (c)Pt/Al_2O_3 monolithic catalysts after hydrothermal aging at 700 °C for 120 h. (d) Comparison of T10, T50 and T90 which denote the temperatures of 10%, 50% and 90% conversion, respectively, over the three hydrothermal-aged DOC catalysts.

272 °C, respectively, while T_{90} values are 330 °C, 316 °C, 316 °C and 455 °C over the washcoat Pt/CeO_2-Al_2O_3 catalysts, respectively. As displayed in Figure S10, a certain degree of sintering took place in Pt nanoparticles after hydrothermal aging, however, ultrafine Pt nanoparticles (average size is about 6.9 nm) can be still observed. As such, a slight reduction of catalytic activities was observed over the Pt(ALD)/CeO_2 nano-array. In terms of wash-coat catalyst after hydrothermal aging, the Pt particles size (average sizes are 23.3 and 18.0 nm) is much bigger than that of nano-array sample. These results illustrate the great potential of Pt(ALD)/CeO_2 nano-array catalysts in practical DOC applications.

For the automotive after-treatment application, catalytic convertors always experience various physical damages originating from the thermal, chemical, and mechanical stresses occurring under unstable engine operating conditions. As a result, the washcoat layers might be broken off from monolithic substrates which decreases the catalyst efficiency due to the lost active materials [68,69]. On the other hand, it is noted that low washcoat loading may be of a greater tendency for poison species to deposit on the catalyst particles or to block the pores. Here the nanoarray monolith has a much smaller thickness compared to the washcoat. Therefore, although the potential deposition of poison species is not part of this study, it could be an interesting subject to work with in the near future. It can be found that the nano-array-based catalyst can much better withstand mechanical stress than the washcoat counterpart due the superior adhesion to the monolith substrate; both the nano-array and washcoat based monolithic catalysts were treated with ultrasound to compare their mechanical stability, and the results are shown in Fig. 9. With the ultrasound vibration, the water that holds the wahscoat sample becomes cloudy only a few seconds, but the water stays clear even after 30 min for the nano-array sample. Consequently, the ultrasound-treated washcoat monolithic catalyst shows increased DOC light-off temperatures by 40–75 °C for both CO and HCs, but there is no significant change in the light-off temperatures in the nano-array catalyst (< 10 °C). These results demonstrated that the nano-array monolithic catalyst has good mechanical stability, offering another advantage in practical applications such as automotive after-treatment.

4. Conclusions

In summary, a new monolithic Pt/CSAO nano-array catalyst was uniformly integrated onto practical 3D-channeled cordierite honeycomb substrates, by combining the self-seeded, additive-free hydrothermal growth of ceria nanoflake arrays and the uniform deposition of spatially distributed, size-controlled Pt nanoparticles by the ALD process. Enabled by the open, hierarchical 3D structure that ensured an efficient mass diffusion as well as the increased, catalytically active exposed Pt nanoparticles and Pt-CeO_2 interfacial areas, the synthesized monolithic Pt/CSAO nano-array catalyst achieved a good low-temperature catalytic oxidation performance over propylene, propane, CO, and NO that featured an ignition temperature as low as 180 °C and the NO oxidation conversion efficiency that reached the thermodynamically predicted limit at the low temperature range down to 200 °C. Overall, the achieved catalytic oxidation performance not only exceeds the performance of the control Pt/CeO_2-Al_2O_3 and Pt/Al_2O_3 washcoat catalyst despite the reduced catalytic material usage but also represents one of the best performance values that have been reported to date. With the superior catalytic oxidation activities and the ultra-high material utilization efficiency, this Pt/CSAO nano-array monolithic catalyst also has a good performance in the simulated LTC-D exhaust as well as mechanical stability, demonstrating a good potential for DOC applications.

Acknowledgements

The authors are grateful for the financial support from the US Department of Energy (Award No. DE-EE0006854) and the US National Science Foundation (Award No. CBET 1344792). A part of research was carried out at the Center for Functional Nanomaterials, Brookhaven National Laboratory (BNL), which is supported by the U.S. Department of Energy, Office of Basic Energy Sciences, under Contract No. DE-SC0012704.

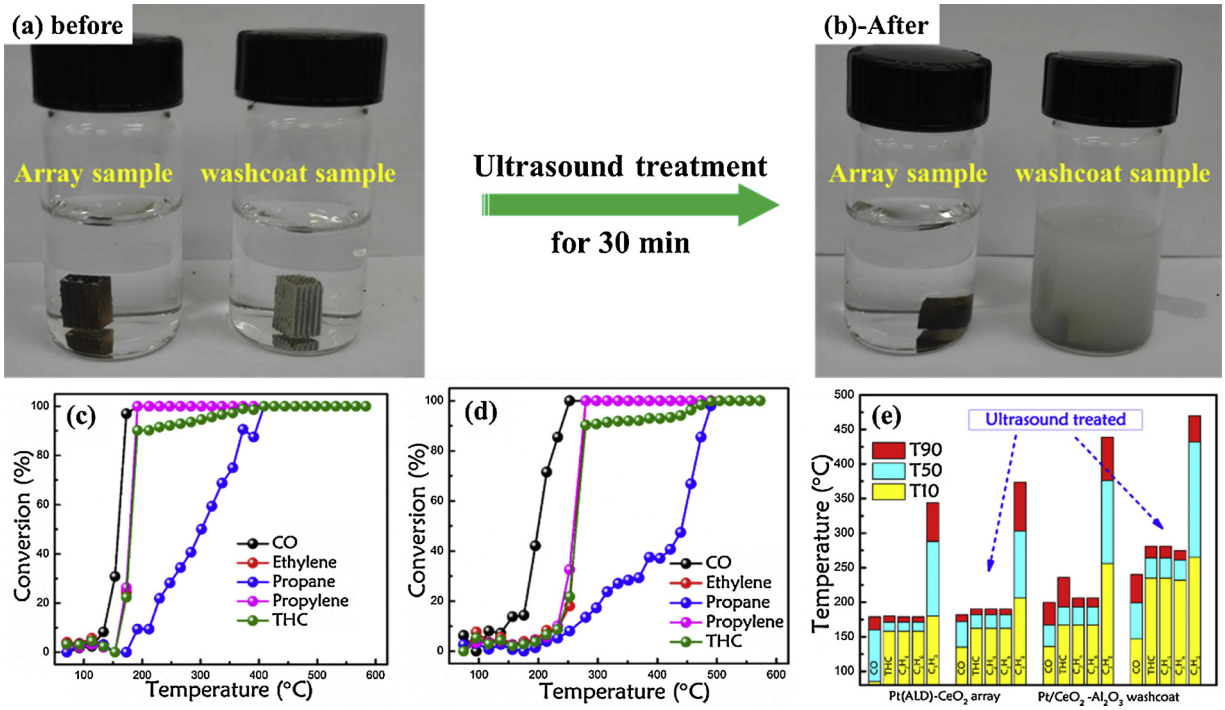

Fig. 9. (a) and (b) photographs of Pt/CeO_2 nano-array and washcoated Pt/CeO_2-Al_2O_3 catalyst before and after ultrasound treatment for 30 min. (c) and (d)DOC activity in the LTC-D simulated exhaust of Pt/CeO_2 nano-array and washcoated Pt/CeO_2-Al_2O_3 catalyst before and after ultrasound treatment for 30 min. (e) Comparison of T10, T50 and T90 over the fresh and ultrasound treated DOC catalysts.

Appendix A. Supplementary data

Supplementary material related to this article can be found, in the online version, at doi:https://doi.org/10.1016/j.apcatb.2019.01.028.

References

[1] H. Yao, Y.Y. Yao, J. Catal. 86 (1984) 254–265.
[2] T. Montini, M. Melchionna, M. Monai, P. Fornasiero, Chem. Rev. 116 (2016) 5987–6041.
[3] F. Wang, M. Wei, D.G. Evans, X. Duan, J. Mater. Chem. A Mater. Energy Sustain. 4 (2016) 5773–5783.
[4] J. Paier, C. Penschke, J. Sauer, Chem. Rev. 113 (2013) 3949–3985.
[5] Y. Guo, Z. Ren, W. Xiao, C. Liu, H. Sharma, H. Gao, A. Mhadeshwar, P.-X. Gao, Nano Energy 2 (2013) 873–881.
[6] P.-X. Gao, Y. Guo, Z. Ren, Ultra-efficient, Robust, and Well-defined Metal Oxide Nano-array Based Monolithic Catalysts for Emisson Control, ABSTRACTS OF PAPERS OF THE AMERICAN CHEMICAL SOCIETY, AMER CHEMICAL SOC 1155 16TH ST, NW, WASHINGTON, DC 20036 USA (2013).
[7] S. Wang, Z. Ren, Y. Guo, P.-X. Gao, CrystEngComm 18 (2016) 2980–2993.
[8] Z. Ren, Y. Guo, P.-X. Gao, Catal. Today 258 (2015) 441–453.
[9] W.X. Tang, P.X. Gao, MRS Commun. (2016) 1–19.
[10] T.P. Senftle, A.C. van Duin, M.J. Janik, ACS Catal. 7 (2016) 327–332.
[11] S. Zhang, C.-R. Chang, Z.-Q. Huang, J. Li, Z. Wu, Y. Ma, Z. Zhang, Y. Wang, Y. Qu, J. Am. Chem. Soc. 138 (2016) 2629–2637.
[12] B. Sarkar, C. Pendem, L.N.S. Konathala, T. Sasaki, R. Bal, J. Mater. Chem. A Mater. Energy Sustain. 2 (2014) 18398–18404.
[13] C. Du, Y. Guo, Y. Guo, X.-q. Gong, G. Lu, J. Mater. Chem. A Mater. Energy Sustain. 3 (2015) 23230–23239.
[14] Z. Ren, V. Botu, S. Wang, Y. Meng, W. Song, Y. Guo, R. Ramprasad, S.L. Suib, P.X. Gao, Angew. Chem. Int. Ed. 53 (2014) 7223–7227.
[15] Y. Guo, G. Liu, Z. Ren, A. Piyadasa, P.-X. Gao, CrystEngComm 15 (2013) 8345–8352.
[16] W. Xiao, Y. Guo, Z. Ren, G. Wrobel, Z. Ren, T. Lu, P.-X. Gao, Cryst. Growth Des. 13 (2013) 3657–3664.
[17] S.-Y. Chen, W. Song, H.-J. Lin, S. Wang, S. Biswas, M. Mollahosseini, C.-H. Kuo, P.-X. Gao, S.L. Suib, ACS Appl. Mater. Interfaces (2016).
[18] Z. Ren, Z. Wu, W. Song, W. Xiao, Y. Guo, J. Ding, S.L. Suib, P.-X. Gao, Appl. Catal. B 180 (2016) 150–160.
[19] S. Wang, Z. Ren, W. Song, Y. Guo, M. Zhang, S.L. Suib, P.-X. Gao, Catal. Today 258 (2015) 549–555.
[20] Y. Guo, Z. Zhang, Z. Ren, H. Gao, P.-X. Gao, Catal. Today 184 (2012) 178–183.
[21] Z. Ren, Y. Guo, Z. Zhang, C. Liu, P.-X. Gao, J. Mater. Chem. A Mater. Energy Sustain. 1 (2013) 9897–9906.
[22] Z. Ren, Z. Wu, W. Song, W. Xiao, Y. Guo, J. Ding, S.L. Suib, P.-X. Gao, Appl. Catal. B 180 (2016) 150–160.
[23] W. Tang, S. Wang, W. Xiao, S. Du, X. Lu, S. Hoang, J. Ding, P.-X. Gao, Catal. Today (2017).
[24] W. Tang, Z. Ren, X. Lu, S. Wang, Y. Guo, S. Hoang, S. Du, P.X. Gao, ChemCatChem 9 (2017) 4112–4119.
[25] Z. Zhang, H. Gao, W. Cai, C. Liu, Y. Guo, P.-X. Gao, J. Mater. Chem. 22 (2012) 23098–23105.
[26] G.-R. Li, D.-L. Qu, X.-L. Yu, Y.-X. Tong, Langmuir 24 (2008) 4254–4259.
[27] X.-h. Lu, D.-z. Zheng, J.-y. Gan, Z.-q. Liu, C.-l. Liang, P. Liu, Y.-x. Tong, J. Mater. Chem. 20 (2010) 7118–7122.
[28] S.M. George, Chem. Rev. 110 (2009) 111–131.
[29] N.P. Dasgupta, C. Liu, S. Andrews, F.B. Prinz, P. Yang, J. Am. Chem. Soc. 135 (2013) 12932–12935.
[30] M. Leskelä, M. Ritala, Angew. Chem. Int. Ed. 42 (2003) 5548–5554.
[31] J. Li, X. Liang, D.M. King, Y.-B. Jiang, A.W. Weimer, Appl. Catal. B 97 (2010) 220–226.
[32] J. Lu, B. Fu, M.C. Kung, G. Xiao, J.W. Elam, H.H. Kung, P.C. Stair, Science 335 (2012) 1205–1208.
[33] L. Yan, R. Yu, J. Chen, X. Xing, Cryst. Growth Des. 8 (2008) 1474–1477.
[34] R. Yu, L. Yan, P. Zheng, J. Chen, X. Xing, J. Phys. Chem. C 112 (2008) 19896–19900.
[35] H. Feng, J.A. Libera, P.C. Stair, J.T. Miller, J.W. Elam, ACS Catal. 1 (2011) 665–673.
[36] S.T. Christensen, H. Feng, J.L. Libera, N. Guo, J.T. Miller, P.C. Stair, J.W. Elam, Nano Lett. 10 (2010) 3047–3051.
[37] J.A. Enterkin, W. Setthapun, J.W. Elam, S.T. Christensen, F.A. Rabuffetti, L.D. Marks, P.C. Stair, K.R. Poeppelmeier, C.L. Marshall, ACS Catal. 1 (2011) 629–635.
[38] J. Lu, B. Fu, M.C. Kung, G. Xiao, J.W. Elam, H.H. Kung, P.C. Stair, Science Washington 335 (2012) 1205–1208.
[39] Y. Zhou, D.M. King, X. Liang, J. Li, A.W. Weimer, Appl. Catal. B 101 (2010) 54–60.
[40] L. Olsson, H. Persson, E. Fridell, M. Skoglundh, B. Andersson, J. Phys. Chem. B 105 (2001) 6895–6906.
[41] M. Crocoll, S. Kureti, W. Weisweiler, J. Catal. 229 (2005) 480–489.
[42] D. Bhatia, R.W. McCabe, M.P. Harold, V. Balakotaiah, J. Catal. 266 (2009) 106–119.
[43] V. Meille, Appl. Catal. A Gen. 315 (2006) 1–17.
[44] P. Avila, M. Montes, E.E. Miro, Chem. Eng. J. 109 (2005) 11–36.
[45] S.Y. Joshi, M.P. Harold, V. Balakotaiah, Chem. Eng. Sci. 64 (2009) 4976–4991.
[46] M.J. Stutz, D. Poulikakos, Chem. Eng. Sci. 63 (2008) 1761–1770.
[47] N. Mladenov, J. Koop, S. Tischer, O. Deutschmann, Chem. Eng. Sci. 65 (2010) 812–826.
[48] S.Y. Joshi, M.P. Harold, V. Balakotaiah, Chem. Eng. Sci. 65 (2010) 1729–1747.
[49] L. Mukadi, R. Hayes, Comput. Chem. Eng. 26 (2002) 439–455.
[50] G. Jacobs, L. Williams, U. Graham, D. Sparks, B.H. Davis, J. Phys. Chem. B 107 (2003) 10398–10404.
[51] X. Wang, D. Liu, S. Song, H. Zhang, J. Am. Chem. Soc. 135 (2013) 15864–15872.
[52] Y. Gao, W. Wang, S. Chang, W. Huang, ChemCatChem 5 (2013) 3610–3620.

[53] S. Aranifard, S.C. Ammal, A. Heyden, J. Phys. Chem. C 118 (2014) 6314–6323.
[54] A. Vita, C. Italiano, C. Fabiano, L. Pino, M. Laganà, V. Recupero, Appl. Catal. B 199 (2016) 350–360.
[55] M. Avila, C. Vignatti, C. Apesteguía, T. Garetto, Chem. Eng. J. 241 (2014) 52–59.
[56] A. Santos, S. Damyanova, G. Teixeira, L.V. Mattos, F.B. Noronha, F.B. Passos, J. Bueno, Appl. Catal. A Gen. 290 (2005) 123–132.
[57] C.-H. Lee, Y.-W. Chen, Ind. Eng. Chem. Res. 36 (1997) 1498–1506.
[58] H.-C. Wu, L.-C. Liu, S.-M. Yang, Appl. Catal. A Gen. 211 (2001) 159–165.
[59] M. Haneda, T. Watanabe, N. Kamiuchi, M. Ozawa, Appl. Catal. B 142-143 (2013) 8–14.
[60] J. Gonzalez-Velasco, M. Gutierrez-Ortiz, J. Marc, J. Botas, M. Gonzalez-Marcos, G. Blanchard, Ind. Eng. Chem. Res. 42 (2003) 311–317.
[61] G. Corro, J.L.G. Fierro, V.C. Odilon, Catal. Commun. 4 (2003) 371–376.
[62] K. Arnby, J. Assiks, P.-A. Carlsson, A. Palmqvist, M. Skoglundh, J. Catal. 233 (2005) 176–185.
[63] K. Arnby, A. Törncrona, B. Andersson, M. Skoglundh, J. Catal. 221 (2004) 252–261.
[64] P. Bera, A. Gayen, M. Hegde, N. Lalla, L. Spadaro, F. Frusteri, F. Arena, J. Phys. Chem. B 107 (2003) 6122–6130.
[65] P. Schmitz, R. Kudla, A. Drews, A. Chen, C. Lowe-Ma, R. McCabe, W. Schneider, C. Goralski, Appl. Catal. B 67 (2006) 246–256.
[66] A. Boubnov, S. Dahl, E. Johnson, A.P. Molina, S.B. Simonsen, F.M. Cano, S. Helveg, L.J. Lemus-Yegres, J.-D. Grunwaldt, Appl. Catal. B 126 (2012) 315–325.
[67] X. Auvray, T. Pingel, E. Olsson, L. Olsson, Appl. Catal. B 129 (2013) 517–527.
[68] A. Cybulski, J.A. Moulijn, Catalysis Reviews—Science and Engineering 36 (1994) 179–270.
[69] V. Tomašić, F. Jović, Appl. Catal. A Gen. 311 (2006) 112–121.